
STATE-OF-THE-ART PERIORBITAL DISTANCE PREDICTION AND DISEASE CLASSIFICATION USING PERIORBITAL FEATURES

George R. Nahass

Ophthalmology and Biomedical Engineering
 University of Illinois Chicago College of Medicine
 Chicago, IL, USA
 gnahas2@uic.edu

Ghasem Yazdanpanah

Ophthalmology
 University of Illinois Chicago College of Medicine
 Chicago, IL, USA

Madison Cheung

Plastic and Reconstructive Surgery
 University of Illinois Chicago College of Medicine
 Chicago, IL, USA

Alexander Palacios

Plastic and Reconstructive Surgery
 University of Illinois Chicago College of Medicine
 Chicago, IL, USA

Jeffrey C. Peterson

Ophthalmology
 University of Illinois Chicago College of Medicine
 Chicago, IL, USA

Kevin Heinze

Ophthalmology
 Cornell University
 New York, NY, USA

Sasha Hubschman

Ophthalmology
 University of Illinois Chicago College of Medicine
 Chicago, IL, USA

Chad Purnell

Plastic and Reconstructive Surgery
 University of Illinois Chicago College of Medicine
 Chicago, IL, USA

Pete Setabutr

Ophthalmology
 University of Illinois Chicago College of Medicine
 Chicago, IL, USA

Ann Q. Tran*

Ophthalmology
 University of Illinois Chicago College of Medicine
 Chicago, IL, USA
 annqtran@uic.edu

Darvin Yi[†]

Ophthalmology and Biomedical Engineering
 University of Illinois Chicago College of Medicine
 Chicago, IL, USA
 dyi9@uic.edu

December 10, 2024

ABSTRACT

Periorbital distances contain crucial information for disease assessment and monitoring of medical interventions. We compared three deep learning models—UNet, DeepLabV3, and the Segment Anything Model—for segmenting periorbital regions and predicting periorbital distances. These models were trained on open-source datasets and evaluated on both healthy and diseased eyes, including patients with Thyroid Eye Disease and various craniofacial syndromes. Our approach

*Corresponding author

[†]Corresponding author

significantly improved upon existing methods, offering robust segmentation even for diseased eyes. Leveraging these predicted distances for disease classification, we found that using segmentation networks as an intermediary step increases the generalizability of classification models, with important implications for ophthalmic plastic and craniofacial surgery.

1 Introduction

The pathology of many diseases including thyroid eye disease (TED), myasthenia gravis, Apert syndrome, Crouzon syndrome, hemifacial microsomia rely on accurate measurements of periorbital distances ([1, 2, 3, 4]). As such, it is commonly routine clinical practice in craniofacial and oculoplastic surgery to manually measure these distances to monitor disease progression and quantify the effect of medical and surgical interventions ([5, 6, 7]). However, manual measurement of periorbital distances is subjective and subject to a large degree of intergrader variability ([5, 8]). To address this variability, many approaches leveraging artificial intelligence (AI) have been proposed in the literature ([1, 7, 8, 9, 10, 11, 12]).

While much progress has been made in this area, there are key limitations of current approaches. For example, Van Brummen et. al. and Rana et. al. trained models on a relatively small number of images and only evaluated images taken by a professional photographer or in a fixed position([8, 11]) Chen et. al. provide a smartphone-based algorithm that achieves good accuracy but is only applicable on ptotic eyelids, requires a high degree of standardization of input images, and only measures MRD 1 and 2 distances ([12]). Furthermore, there is an absence of literature utilizing periorbital distances to predict disease status.

Here, we set out to evaluate multiple deep learning approaches for oculoplastic segmentation, including the Segment Anything Model (SAM), a foundational model for segmentation ([13]). Here, we leverage open-source datasets and demonstrate that networks trained on large amounts of images of healthy eyes can be adequately used for the segmentation of diseased eyes. We evaluate our models on multiple clinical imaging datasets captured under different conditions and achieve state-of-the-art performance periorbital distance predictions on all datasets evaluated here. Furthermore, we demonstrate that periorbital distances measured using our pipeline can be effectively used for downstream classification tasks. This study establishes new benchmarks for periorbital distance prediction and provides a highly accurate and reliable technique for the objective quantification of these distances, which has implications in both management and diagnosis of oculoplastic and craniofacial disorders.

2 Methods

2.1 Datasets

For training UNET and DeepLabV3 models we used 30,000 images from the open-source CelebAMask dataset ([14]). For testing, we used 827 images from the open-source Chicago Facial Dataset (Healthy) as our healthy controls, 113 images of Thyroid Eye Disease (TED) patients from the UIC Ophthalmology outpatient clinic, and 155 images of patients with various craniofacial disorders affecting the eyes such as Apert, Crouzon, hemifacial microsomia, Goldenhaar syndrome, and more from the UIC Craniofacial Center (Craniofacial)([15, 16, 17]). Craniofacial images were taken by a trained photographer, and TED images were captured during routine clinic visits on a smartphone. All images were rotated so that the line between the nasion and midpoint of the hairline was vertical prior to downstream use. See Table 1 for a complete description of the datasets used in this study.

Dataset	# Images	Disease Status	Source	Utility
Craniofacial	155	Mix of craniofacial disorders	UIC Craniofacial Center	Testing
TED	113	Thyroid Eye Disease	UIC Ophthalmology Clinic	Testing
Healthy	827	None	Open Source (Chicago Facial Dataset)	Testing
Celeb	30,000	None	Open Source (CelebAMask-HQ)	Training

Table 1: Details of all imaging datasets used in this study. ‘# Images’ denotes the number of images used in evaluating the various pipelines, ‘Source’ indicates where the data was acquired from, and ‘Utility’ indicates the role of the dataset in our models. UNET and DeepLabV3 were trained on the CelebAMask dataset, but these images were not included in any test sets. The craniofacial dataset contains a range of diseases and syndromes such as Aperts, Crouzons, Goldenhar, and hemifacial microsomia.

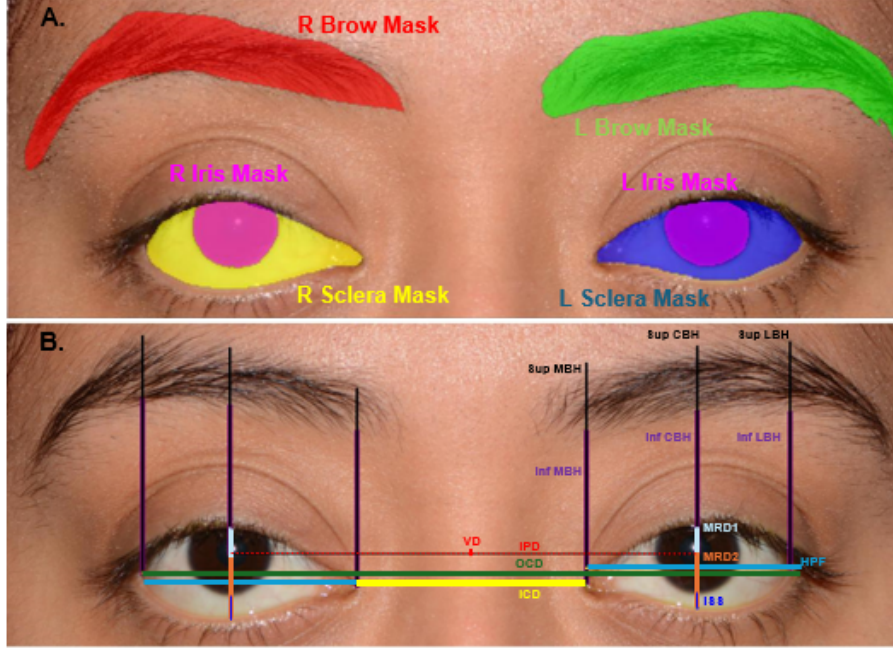


Figure 1: Representative example of ground truth segmentation masks and periorbital distance prediction. A): Ground truth masks of the anatomical regions used for evaluating segmentation results and deriving ground truth distance measurements on the face. B). Distance measurements calculated from (A). Pixels were converted to mm using 11.71 mm as the standard diameter for the iris. Scleral area was calculated by taking the ratio of sclera mask to the iris mask, and 4th degree polynomials were fit to the superior and inferior scleral margin. Abbreviations are as follows: VD- Vertical Dystopia, IPD-Inner Pupil Distance, OCD-Outer Canthal Distance, ICD-Inner Canthal Distance, HPF-Horizontal Palpebral Fissure, MRD-Margin to Reflex Distance, ISS- Inferior Scleral Show. Other measurements not shown are VP-VPF-sum of MRD 1 and 2, canthal height-distance between inner pupillary line and medial/lateral canthus, canthal tilt, and scleral area.

2.2 Generation of Ground Truth Images

All ground truth segmentation masks were generated by trained annotators (3 medical students) using the Computer Vision Annotation Tool (CVAT). For sclera annotation, annotators were instructed to annotate from the lateral canthus to the medial canthus, including the caruncle. Ground truth periorbital distances were generated using the same pipeline to extract the anatomical distances from segmentation masks produced by the deep learning networks. An example of ground truth segmentation masks from CVAT and resultant periorbital distances can be seen in Figure 1.

2.3 U-NET and DeepLabV3 Pipeline.

All images and annotations were cropped to only have the eyes in frame using MediaPipe face mesh coordinates. For training, images were split at the midline to separate the left and right eyes. Both sides of the image were then resized to be 256x256. The network was trained for brow and eye segmentation using cross-entropy loss and Adam optimization for 5000 epochs with a learning rate of .01 and β 1 and 2 of .5 and .99, respectively. SAM was used to generate segmentation masks for the iris using bounding boxes obtained by MediaPipe Facemesh ([18]). All segmentation masks were then used to predict periorbital distances using standard computer vision processing techniques described below. Segmentation quality was evaluated using the Dice score according to Equation 1. The whole pipeline can be seen in Figure 2.

$$Dice = \frac{2(\mathbf{X} \cap \mathbf{Y})}{|\mathbf{X}| + |\mathbf{Y}|} \quad (1)$$

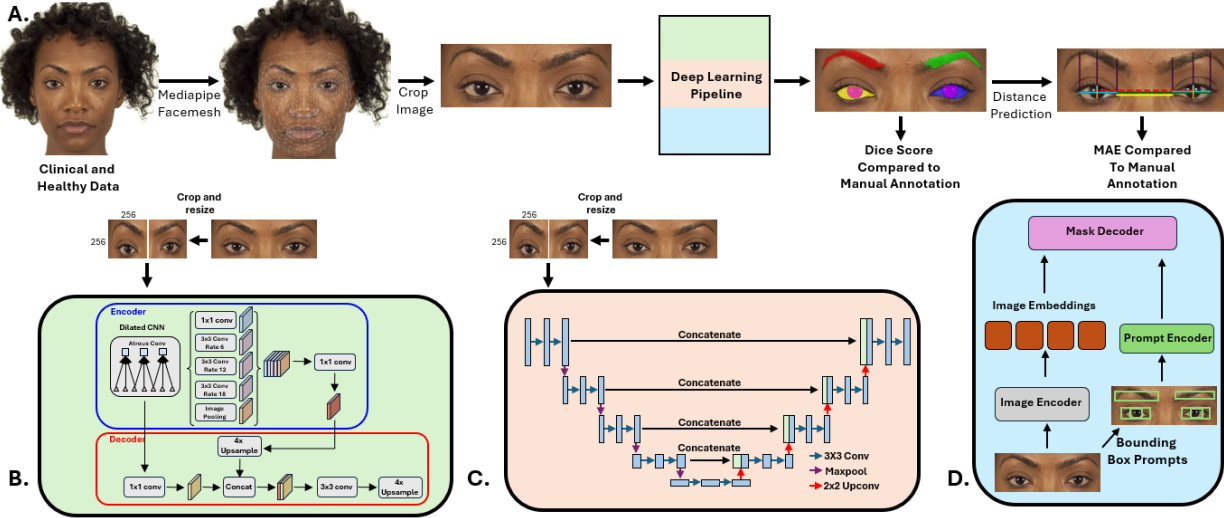


Figure 2: Graphical schematic of segmentation models and distance prediction pipelines. A) Input images of an entire face enter the pipeline and are fit with a Facemesh using MediaPipe. The image is then cropped around the eyes and segmented using one of the three deep learning models (described in 1B-D). Following segmentation, the Dice score was calculated, and the segmentation masks are used to predict periorbital distances which were compared to distances obtained from human annotations using the mean absolute error. B-C) Graphical schematic of the DeepLabV3 and UNET architectures used. In both models, input images are initially cropped at the midline and both eyes are resized to be 256x256 prior to segmentation. DeepLabV3 and UNET models were trained for brow and sclera segmentation on the CelebAMask open source dataset. D) Graphical schematic of the Segment Anything Model (SAM). The cropped image was used as input, and bounding box prompts were derived from MediaPipe facemesh coordinates. Resulting segmentation maps from all pipelines were then used for downstream distance prediction.

2.4 Foundational Model Pipeline

A 468-point face mesh was fit to every input facial image using MediaPipe. Using the MediaPipe coordinates, bounding boxes were obtained for both left and right scleras, brows, and irises. Additionally, the image was also cropped around the ocular anatomy. These bounding boxes were then submitted to SAM for segmentation. The open source `vit_h` weights of SAM were used. Resultant segmentation masks were then used to predict periorbital distances using standard computer vision processing techniques described below. The whole pipeline can be seen in Figure 2.

2.5 Calculation of Anatomical Relationships

The iris diameter was set to a scale of 11.71 millimeters (mm), which was used to derive pixel to mm conversions as described by Van Brummen ([8]). Measurements for inferior and superior scleral show were obtained by calculating the distance from the inferior and superior iris to the inferior lid, respectively. Margin to Reflex Distance 1 and 2 (MRD 1 and 2) were calculated as the distance from the center of the iris to the superior or inferior lid.

Inner canthal distance (ICD), outer canthal distance (OCD), and interpupillary distance (IPD) were determined by the horizontal distance of the bounding box between the medial canthus, lateral canthus, and iris center, respectively. Brow heights were obtained by measuring the distance between the medial canthus, lateral canthus, and iris center to their respective brow points. Brow points were identified as the point on the brow with the same x coordinate as the medial canthus, lateral canthus, or iris center depending on the measurement being acquired.

Canthal tilt was calculated as the angle between the line running through the medial canthus perpendicular to the vertical line of the face, defined by the soft tissue nasion and the midpoint of the hairline, and the line between the medial and lateral canthus. Vertical dystopia was calculated by drawing a line from the medial canthus to the vertical line between the soft tissue nasion and the midpoint of the hairline of both the left and right eye. The Euclidean distance between the intersection of the left medial canthus and the vertical line of the face and the intersection of the right medial canthus and the vertical line of the face determined the extent of the vertical dystopia. Medial and lateral canthal height was

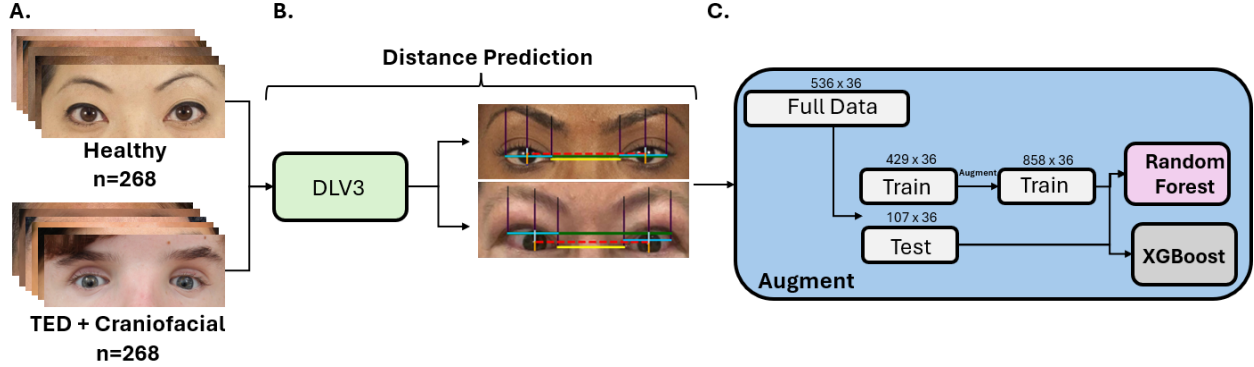


Figure 3: 268 images were randomly sampled from the healthy dataset, and the ‘diseased’ dataset was created by combining TED and craniofacial images. This dataset was split 80/20 for training testing. B) Periorbital distances were predicted for both healthy and diseased datasets using DeepLabV3. C) The resultant distances were then used to train and test XGBoost and random forest models. Details on training methodology can be found in the methods section.

defined as the distance between the medial and lateral canthus to the line between the iris centers. Vertical palpebral fissure was computed as the sum of MRD 1 and 2. The horizontal palpebral fissure was defined by the horizontal distance of the bounding box between the medial canthus and the lateral canthus. Scleral area was calculated as the ratio of the iris to the sclera segmentation masks. A labeled diagram of all periorbital distances measured can be seen in Figure 1.

2.6 Comparison to PeriorbitAI

The open-source code and weights for PeriorbitAI were obtained. The source code was modified to have all measurements initialized as 0 to prevent the algorithm from stopping in the event of failed prediction. All testing data was cropped to include the nose and forehead and resized using bilinear interpolation as described in the original paper. 8. PeriorbitAI was then run on all of our testing datasets (Table 1). All anatomic measurements were calculated using the same methodologies described in Van Brummen et. al. to permit fair comparisons.

The percentage of images that failed analysis for any given measurement was recorded along with the MAE compared to distances from human annotations. For all measurements, MAE for both our models as well as PeriorbitAI was computed using only images successfully analyzed by PeriorbitAI. For example, if PeriorbitAI failed to predict right MRD 1 on a certain patient, the resulting ‘0’ value would be excluded from the PeriorbitAI analysis, and this patient’s right MRD 1 would also be excluded from the MAE computation of our models for comparison purposes.

2.7 Hardware and Statistical Analysis

All batch experiments were performed on 3 Nvidia 1080Ti GPUs. Statistical analysis and other machine learning experiments were performed on an AMD Ryzen 7 7800x3D CPU. All code was written in Python 3.8. Statistical analysis was performed in Python. Mean absolute error for all measurements was calculated according to Equation 2. Bland Altman plots were used to compare the pixel level measurements predicted by the deep learning models to the measurements derived from the human annotations. For each periorbital measurement, the mean was plotted against the difference between the human and deep learning prediction. The mean difference and the 95 percent limits of agreement (mean difference \pm 1.96 standard deviations) were calculated. The percentage of measurements falling outside the limits of agreement was also computed.

$$MAE = \frac{1}{n} \sum_{i=1}^n |\hat{y}_i - y_i| \quad (2)$$

2.8 Machine Learning Classification

Both random forest and XGBoost models were trained for disease classification using the predicted distances from DeepLabV3. TED and Craniofacial datasets were combined to create the ‘Disease’ class ($n = 268$), and 268 images

		MRD 1	MRD 2	ICD	IPD	OCD	ISS	SSS	Vert Fissure	Horiz Fissure	Med Canthal	Lat Canthal
Healthy	UNET	0.41 ± 0.27	0.60 ± 0.29	2.30 ± 1.46	0.46 ± 1.18	2.07 ± 1.69	0.27 ± 0.28	0.00 ± 0.02	0.90 ± 0.39	1.05 ± 0.82	0.57 ± 0.36	0.50 ± 0.29
	DLV3	0.32 ± 0.23	0.63 ± 0.29	3.60 ± 1.80	0.46 ± 1.18	1.38 ± 1.78	0.32 ± 0.31	0.00 ± 0.01	0.81 ± 0.34	2.14 ± 1.25	0.70 ± 0.43	0.51 ± 0.30
	SAM	0.61 ± 0.56	0.44 ± 0.40	2.51 ± 2.68	0.66 ± 1.11	2.89 ± 3.17	0.19 ± 0.32	0.02 ± 0.12	0.76 ± 0.76	2.34 ± 1.78	0.68 ± 0.52	0.64 ± 0.50
TED	UNET	0.72 ± 0.66	0.74 ± 0.72	3.74 ± 3.73	2.68 ± 2.96	3.79 ± 4.33	0.37 ± 0.64	0.19 ± 0.47	0.95 ± 1.16	2.30 ± 2.46	0.72 ± 0.53	0.78 ± 0.51
	DLV3	0.66 ± 0.59	0.62 ± 0.55	2.51 ± 2.44	2.68 ± 2.96	3.89 ± 4.34	0.32 ± 0.50	0.14 ± 0.38	0.73 ± 0.84	1.83 ± 1.85	0.70 ± 0.48	0.79 ± 0.49
	SAM	0.91 ± 0.75	1.12 ± 1.10	4.33 ± 4.05	2.50 ± 2.64	5.20 ± 3.65	0.74 ± 0.98	0.22 ± 0.45	1.73 ± 1.59	3.42 ± 2.82	0.83 ± 0.60	0.90 ± 0.54
Craniofacial	UNET	0.47 ± 0.28	0.58 ± 0.42	2.00 ± 2.72	2.33 ± 3.29	3.79 ± 5.29	0.15 ± 0.30	0.00 ± 0.01	0.50 ± 0.46	1.73 ± 2.11	0.61 ± 0.47	0.68 ± 0.48
	DLV3	0.47 ± 0.28	0.53 ± 0.39	1.47 ± 2.39	2.33 ± 3.29	3.84 ± 4.40	0.13 ± 0.25	0.00 ± 0.01	0.45 ± 0.42	1.62 ± 1.25	0.61 ± 0.38	0.63 ± 0.44
	SAM	0.58 ± 0.45	0.68 ± 0.60	2.16 ± 2.38	2.30 ± 3.04	4.05 ± 3.82	0.25 ± 0.50	0.02 ± 0.13	0.81 ± 0.80	1.76 ± 1.55	0.58 ± 0.42	0.83 ± 0.59

Table 2: Mean Absolute Error (MAE) of all models on all datasets used in this study for eye measurements. MAE was calculated according to Equation 2, and is reported as +/- the standard deviation. Bold indicates the lowest MAE for each measurement for each model. Bilateral distances were averaged. Abbreviations can be interpreted as follows: MRD-Margin to Reflex Distance, ICD-inner canthal distance, IPD-interpupillary distance, OCD- outer canthal distance, ISS- inferior scleral show, SSS- superior scleral show, Vert Fissure- vertical palpebral fissure, Horiz Fissure- horizontal palpebral fissure, Med Canthal- medial canthal height, Lat Canthal- lateral canthal height.

were randomly sampled from the Healthy dataset to prevent class imbalance. The entire set of features ($n = 36$) from the DeepLabV3 pipeline were used for training. The dataset was then augmented by reversing the order of left and right measurements to double the size of the training set. In both pipelines, optimal hyperparameters for each individual model were determined using grid search in scikit-learn. The whole pipeline can be seen in Figure 3. Accuracy, precision, and recall were computed according to Equation 3. Area under the receiver operator characteristic curve was computed using scikit-learn in Python.

For comparison purposes, a ResNet50 pretrained on ImageNet1K was finetuned using the same dataset. The final layer was modified to have two output nodes, and the network was trained for 10 epochs using an Adam optimizer with a learning rate of .0001 and a batch size of 8. An 80/20 train/ test split was used for all models.

$$\text{Acc} = \frac{TP + TN}{TP + TN + FP + FN}, \quad \text{Pr} = \frac{TP}{TP + FP}, \quad \text{Re} = \frac{TP}{TP + FN} \quad (3)$$

3 Results

3.1 Evaluation of Segmentation

The median Dice scores of the iris, sclera, and brow segmentation in all datasets was greater than .9 using SAM (Supplemental Figure 1A). As the CelebAMask dataset does not have iris annotations, SAM was used for iris segmentation in all downstream pipelines. It has been reported elsewhere that SAM is highly robust for iris segmentation, even outperforming human annotators ([19]).

We trained a UNET and DeepLabV3 model for brow and sclera segmentation using the CelebAMask dataset with different size train sets (Supplemental Figure 1B-H). For brow and sclera segmentation, superior segmentation was achieved using the UNET and DeepLabV3 model compared to SAM with lower variation across the entire dataset. Additionally, our data suggests that there is minimal difference when training on 1000 images vs 25,000 for brow and sclera segmentation.

3.2 Distance Prediction Accuracy

We evaluated the predicted periorbital distances in two steps: first on a pixel-level basis prior to conversion to mm using the diameter of the iris, and second following conversion to mm.

3.2.1 Pixel Level Evaluation

Bilateral measurements were averaged to evaluate the pixel distances, and Bland Altman plots were created to compare the human annotations to the AI predictions (Supplemental Figures 2 and 3). We quantified the quality of predicted distances by measuring the percentage of points outside the limits of agreement (LOA). For MRD 1, MRD 2, ISS, and SSS on TED images, the lowest percentage of images with measurements outside the LOA was 2.6, 5.16, 4.55, and 0. For MRD 1, MRD 2, ISS, and SSS on Craniofacial images, the lowest percentage of images with measurements outside the LOA was 6.19, 4.42, 2.7, and 2.68. Full results for the percentage outside the LOA for eyes and brows can be found in Supplemental Table 1-2. DeepLabV3 most often had the lowest percentage of measurements outside the limits of agreement on all datasets.

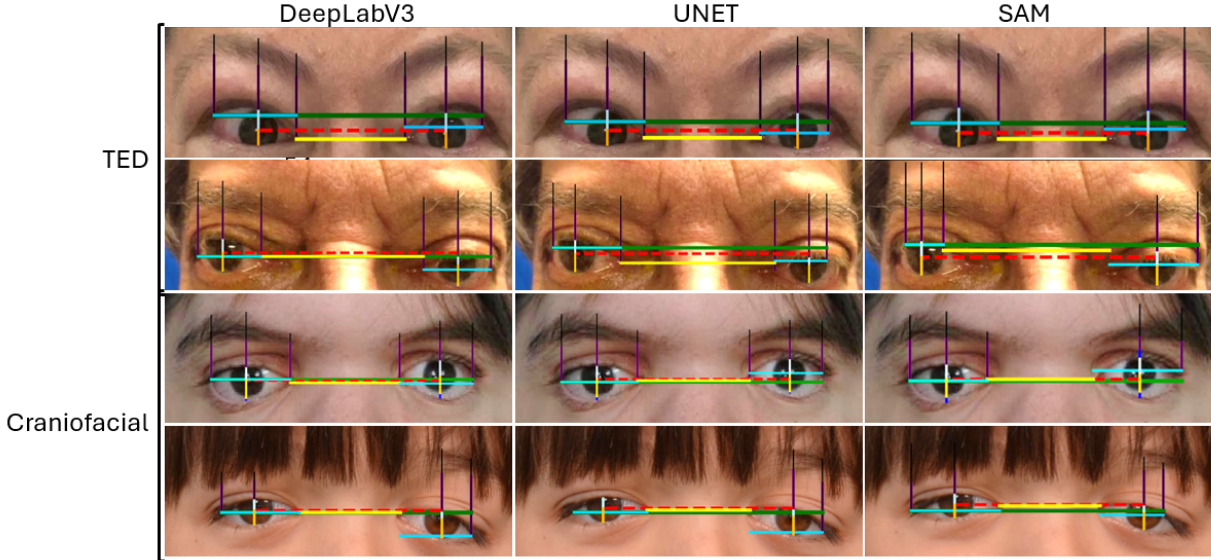


Figure 4: Qualitative evaluation of all three models periorbital distance prediction. Predicted distances from DeepLabV3, UNET, and SAM (left to right columns) for TED and craniofacial datasets (rows 1-2 and 3-4, respectively). Brightness has been increased on some images for presentation purposes only. Color can be interpreted as follows: Red dashes: IPD, teal: HPF, light blue: MRD 1, orange: MRD 2, green: OCD, yellow: ICD, purple: Inferior brow height, black: Superior brow height.

3.2.2 Millimeter Level Evaluation

The MAE was computed for every model on every dataset to evaluate the accuracy on a mm level. The DeepLabV3 pipeline most consistently had the lowest error rate Table 2. It is documented in the literature that the average variation between human annotators for MRD 1 and 2 can be up to .5 mm, and up to 4mm for distances between the canthi both ICD and OCD 8. Using these as benchmarks, the MAE of our deep learning predicted distances is less than or very close to the error observed between trained human annotators. For example, the best MAE for MRD 1 on TED and Craniofacial images is .6 and .47, respectively, and for MRD 2, .62 and .63, respectively. The MAE reported for ICD on TED and Craniofacial images is 2.51 and 1.47, respectively, and 3.79 for OCD on TED and Craniofacial images. The full results of the MAE of eye measurements can be seen in Table 2, and the full distribution of error across all models and all datasets can be seen in Supplemental Figure 4.

The MAE of brow distances can be found in Supplemental Table 3. A long-tailed MAE distribution of brow height MAE was observed (Supplemental Figure 5). This is due to discrepancies in how human annotators define the brow margin versus the segmentation pipeline. Examples of how the differences in human annotation or insufficient medial sclera segmentation can lead to such high variance in brow height can be seen in Supplemental Figure 8. To fairly evaluate the brow height without these relatively rare discrepancies, we removed all brow heights greater than 1 STD above the mean and recalculated the MAE (Supplemental Table 4). In this analysis, the MAE decreased significantly to levels comparable with the variance in human annotators. Full representative distance annotations of both the eye and brow can be seen for all models for all datasets in Figure 4.

3.3 Comparison to PeriorbitAI

We compared our pipelines to the current state-of-the-art (SOTA) method for periorbital distance prediction, PeriorbitAI 8. PeriorbitAI failed to process our entire dataset. For eyes in the Healthy, TED, and Craniofacial datasets, the average number of images successfully analyzed is 85%, 59%, and 67% respectively. When comparing the same images successfully analyzed by PeriorbitAI to our pipelines, we achieved superior performance in all but one measurement on one dataset (OCD on TED) (Table 3). Our models also achieved superior brow performance on all but one brow height (Sup. Medial on Craniofacial) compared to PeriorbitAI (Supplemental Table 5).

		Right				Left					
		MRD 1	MRD 2	Lat Canthal	Med Canthal	MRD 1	MRD 2	Lat Canthal	Med Canthal	ICD	OCD
Healthy	% Dataset periorbitAI	0.85	0.85	0.94 ± 0.75	0.71 ± 0.60	1.08 ± 0.88	0.50 ± 0.47	0.79 ± 0.63	0.73 ± 0.60	3.82 ± 3.99	4.99 ± 4.09
	SAM	0.59 ± 0.65	0.45 ± 0.44	0.67 ± 0.66	0.69 ± 0.62	0.61 ± 0.74	0.43 ± 0.58	0.63 ± 0.62	0.66 ± 0.63	2.44 ± 2.63	2.86 ± 3.18
	UNET	0.42 ± 0.35	0.62 ± 0.39	0.49 ± 0.39	0.57 ± 0.46	0.37 ± 0.32	0.60 ± 0.34	0.49 ± 0.39	0.55 ± 0.44	2.30 ± 1.48	2.06 ± 1.67
	DLV3	0.35 ± 0.32	0.68 ± 0.40	0.51 ± 0.43	0.72 ± 0.55	0.30 ± 0.28	0.61 ± 0.34	0.50 ± 0.40	0.67 ± 0.51	3.60 ± 1.80	1.37 ± 1.79
TED	% Dataset periorbitAI	0.60	0.58	1.15 ± 1.18	1.00 ± 0.89	1.10 ± 1.62	0.90 ± 1.09	1.29 ± 1.35	1.05 ± 1.13	7.12 ± 5.30	3.07 ± 2.89
	SAM	0.77 ± 0.84	0.84 ± 0.96	0.84 ± 0.61	0.62 ± 0.59	0.86 ± 1.07	1.38 ± 1.81	1.01 ± 0.74	0.84 ± 0.81	4.06 ± 3.85	4.85 ± 3.13
	UNET	0.61 ± 0.67	0.57 ± 0.58	0.67 ± 0.69	0.65 ± 0.64	0.58 ± 0.77	0.64 ± 0.72	0.87 ± 0.76	0.63 ± 0.63	2.82 ± 2.36	3.22 ± 2.52
	DLV3	0.57 ± 0.59	0.54 ± 0.60	0.67 ± 0.64	0.73 ± 0.64	0.57 ± 0.76	0.53 ± 0.42	0.81 ± 0.70	0.59 ± 0.54	2.29 ± 2.43	3.76 ± 2.36
Craniofacial	% Dataset periorbitAI	0.75	0.66	0.83 ± 0.59	0.84 ± 0.69	1.39 ± 1.38	0.71 ± 0.77	0.91 ± 0.80	0.78 ± 0.77	3.91 ± 3.42	3.22 ± 2.82
	SAM	0.50 ± 0.44	0.64 ± 0.60	0.78 ± 0.67	0.61 ± 0.48	0.59 ± 0.68	0.75 ± 0.95	0.92 ± 0.85	0.55 ± 0.60	1.83 ± 1.75	4.09 ± 3.05
	UNET	0.46 ± 0.40	0.58 ± 0.42	0.67 ± 0.58	0.66 ± 0.63	0.41 ± 0.31	0.52 ± 0.40	0.60 ± 0.56	0.49 ± 0.52	1.39 ± 1.62	2.84 ± 2.33
	DLV3	0.46 ± 0.40	0.55 ± 0.42	0.63 ± 0.54	0.66 ± 0.54	0.41 ± 0.31	0.45 ± 0.37	0.58 ± 0.49	0.52 ± 0.41	0.93 ± 0.94	3.31 ± 2.29

Table 3: Comparison of MAE (Equation 2) of our models to PeriorbitAI for eye measurements. For all measurements, for both our models and PeriorbitAI, MAE was computed using only images successfully analyzed by PeriorbitAI. ‘% Dataset’ denotes the percentage of the original dataset for each measurement successfully processed by PeriorbitAI. Bold denotes lowest MAE of each measurement for each dataset. Abbreviations can be interpreted as follows: MRD-Margin to Reflex Distance, ICD-inner canthal distance, IPD-interpupillary distance, OCD- outer canthal distance, ISS- inferior scleral show, SSS- superior scleral show, Vert Fissure- vertical palpebral fissure, Horiz Fissure- horizontal palpebral fissure, Med Canthal- medial canthal height, Lat Canthal- lateral canthal height.

	Accuracy	Precision	Recall	AUROC
XGBoost	0.93	0.96	0.89	0.98
Random Forest	0.94	0.96	0.93	0.98
CNN	1.00	1.00	1.00	1.00

Table 4: Results of training random forest and XGBoost models on predicted periorbital distances. CNN denotes a ResNet50 used for comparison. Full details of the protocol can be found in the methods. Bold denotes maximum score. Accuracy, precision, and recall were computed according to Equation 3.

3.4 Periorbital Distances for Disease Classification

We trained two machine learning models to evaluate whether the predicted periorbital distances can be used for disease classification (Figure 3). We initially created a dataset by combining TED and Craniofacial images into a ‘Disease’ class and then randomly sampled 268 images from the ‘Healthy’ dataset for binary classification. As the DeepLabV3 pipeline had the lowest error on average across all datasets, we only evaluated distances produced from it in model training. We trained both random forest (RF) and XGBoost (XGB) models and compared the classification results to a convolutional neural network.

While the CNN performed the best, achieving perfect performance in every metric evaluated, highly competitive performance was achieved by the random forest model, achieving accuracy, precision, recall, and area under the receiver operating characteristic curve values of .94, .96, .93 and .98 respectively (Table 4).

4 Discussion

Prior work has attempted to automate the calculation of periorbital distances. Shao et al. presented a segmentation pipeline to analyze multiple components of eyelid morphology in TED patients as well as predict MRD 1 and 2 with very high accuracy, and Chen et al. published a smartphone-based deep learning method to predict MRD 1, MRD 2, and levator muscle function ([12, 20]) Rana et. al. developed a segmentation network for periorbital distance prediction on healthy eyes and evaluated the effect on different ethnic groups ([11]) Van Brummen et. al. presented PeriorbitAI, a deep learning model to predict a full suite of periorbital distances across a wider range of diseases. While PeriorbitAI achieved good performance, they still only evaluated images captured in a standardized position and evaluated a relatively low number of images (n=41) ([8])

In this study, the authors set out to build a pipeline that was compatible with a wide range of craniofacial and ophthalmic diseases, as well as on ‘in the wild’ captured images. Three models were evaluated (SAM, DeepLabV3, and UNET)

for segmentation on open-source images from Chicago Facial Database (Healthy) ([15, 16, 17]) and were used from multiple clinical databases. We trained our DeepLabV3 and UNET models on 30,000 images from the open-source CelebAMask dataset14 and demonstrated that models trained on this open-source dataset can perform excellent segmentation on images with diverse pathology (Supplemental Figure 1).

Additionally, this study utilizes SAM, a massive foundational segmentation model from Meta for this use case. While SAM was capable of impressive segmentation results on our disease datasets (mean Dice score of .85 and .91 on TED and Craniofacial sclera segmentation, respectively), both the UNET and DeepLabV3 models trained with 1000 images performed better. As such, while foundational vision models clearly have large potential clinical utility in this space, utilizing more traditional segmentation backbones using open-source data is still advisable.

In our pipelines, the segmentation mask produced by the network is an intermediary step before distance prediction. We evaluated the predicted distances before and after conversion to mm as evaluation of the pixel level distances to avoid propagation of error resulting from poor iris segmentation (Supplemental Figure 2-3). By quantifying the percentage of measurements outside the 95% LOA of Bland-Altman plots, we can statistically analyze the accuracy and reliability of our segmentation algorithm. For both eye and brow measurements, we see a very low percentage of measurements outside the LOA, indicating that, on average, our models' predictions at the pixel level are in firm agreement with the human-annotated images (Supplemental Tables 1-2). It is documented in the literature that the average variation between human annotators for MRD 1 and 2 can be up to .5 mm and up to 4mm for distances for ICD and OCD and up to 2 mm for brow heights. This implies that there is a wide variation in the 'ground truth' annotations for periorbital measurements. This is due to factors such as ambiguity in the superior and inferior margins of the lids and brows, and challenges in the annotation process resulting from poor image quality. We found that the error of our models was within the range of human graders and was able to predict many of the distances with < .5mm of error. On average, the DeepLabV3 pipeline performed the best across all the datasets achieving the lowest MAE (Table 2, Supplemental Table 3).

An example of how the inherent variability in ocular annotation affects the analysis of periorbital distance prediction can be seen in our brow height calculations. We observed long tailed distributions when looking at brow MAE (Supplemental Figure 5). This is due to how brow heights are dependent on the vertical line from either the medial canthus, iris center, or lateral canthus. If, in the annotation process, an annotator determined the medial or lateral border of the brow to be not in the plane of the medial or lateral canthus, the reported error will be large. While this affects the reported accuracy, upon qualitative comparison images that suffer from this ambiguity, there may be multiple correct interpretations of where the brow margins begin and end (Supplemental Figure 6). The same error will happen if a brow is determined to not be present (or vice versa) by either the annotator or the deep learning model.

To evaluate our model's performance in the context of the field, we compared all our methods to PeriorbitAI, the current SOTA method. PeriorbitAI failed to analyze a large portion of our datasets, and when comparing the same images analyzed in our pipelines, at least one of our models outperforms PeriorbitAI in all but one category (OCD) on Healthy images. Of our datasets, PeriorbitAI performed the best on the Healthy dataset, whereas our models do not compromise performance between Healthy, TED, or Craniofacial datasets (Table 3).

While predicting periorbital distances to a high degree of accuracy has potential clinical utility for tracking disease progression and monitoring the effects of surgical and medical treatment, we hypothesized that these measurements may also be used as features in machine learning models for disease classification. Prior work in oculoplastic disease classification has focused on TED diagnosis from external images ([21, 22, 23]), malignant tumors ([24]), as well as prediction of postoperative outcomes following surgical intervention ([25, 26]). However, to our knowledge no studies have yet explored using periorbital distances directly as features for disease classification. The TED and Craniofacial datasets were grouped into one class called 'Disease', and we trained two machine learning models for classification with our 'Healthy' dataset (Figure 3, Table 4).

While there was a small cost in performance for disease classification when training using the periorbital distances compared to a convolutional neural network (CNN), our approach does provide some explicit technical benefits compared to more conventional models like CNNs. In general, image classification models are highly susceptible to the out-of-distribution (OOD) problem, where performance sharply decreases when testing on data that is OOD to the training set ([27]). Segmentation models, on the other hand, are much more robust to OOD effects as the classification of individual pixels is a local process compared to whole image classification([28]). Furthermore, we have demonstrated that robust segmentation can be achieved on pathologic images when training on open-source, healthy images. Owing to the scarcity of large oculoplastic or craniofacial datasets as well as the OOD challenge faced by conventional classification approaches, using periorbital distances computed through an intermediary segmentation step provides an attractive and scalable strategy for oculoplastic and craniofacial disease classification.

5 Conclusions

The major limitations of this study stem from the size of the Craniofacial and TED dataset. While we have more images in our training set than other studies, benchmarking our model on more images would provide further confidence in its generalizability. Detailed diagnosis were not included in our datasets. Better labeled datasets of a wider range of craniofacial and oculoplastic conditions would allow for a better understanding of how robust our segmentation model is to OOD samples when trained on the CelebAMask dataset and permit more clinically relevant classification experiments. The authors only evaluate binary classification between diseased and healthy eyes, but going forward, we hope to show the utility of periorbital measurements for classification on a more granular diagnostic level. Additionally the CelebAMask dataset was not designed with medical use cases in mind. As such, many images in this dataset have sclera annotations that bleed into the lids or sclera annotations that do not extend to the caruncle medially. Development of large, open-source oculoplastic datasets will allow for higher fidelity segmentation of relevant anatomy, and this work is underway in our group.

References

- [1] Meelis Lootus, Lulu Beatson, Lucas Atwood, Theo Bourdais, Sandra Steyaert, Chethan Sarabu, Zeenia Framroze, Harriet Dickinson, Jean-Christophe Steels, Emily Lewis, Nirav R. Shah, and Francesca Rinaldo. Development and assessment of an artificial intelligence-based tool for ptosis measurement in adult myasthenia gravis patients using selfie video clips recorded on smartphones. *Digital Biomarkers*, 7(1):63–73, 2023.
- [2] Sergey Lvovich Kabak, Nina Alexandrovna Savrasova, Valentina Vladimirovna Zatochnaya, and Yuliya Michailovna Melnichenko. Hemifacial microsomia: skeletal abnormalities evaluation using CBCT (case report). *Journal of Radiology Case Reports*, 13(11):1–9, 2019.
- [3] Vaneshri Chetty, Samer E. Haber, Roman Hossein Khonsari, and Eric Arnaud. Improvement of periorbital appearance in apert syndrome after subcranial le fort III with bipartition and distraction. *The Journal of Craniofacial Surgery*, 31(3):711–715, 2020.
- [4] Diego Strianese, Adriana Iuliano, Mariantonio Ferrara, Chiara Comune, Immacolata Baronissi, Pasquale Napolitano, Alessia D’Alessandro, Piergiacomo Grassi, Giulio Bonavolontà, Paola Bonavolontà, Antonio Sinisi, and Fausto Tranfa. Methotrexate for the treatment of thyroid eye disease. *Journal of Ophthalmology*, 2014:128903, 2014.
- [5] K Boboridis, A Assi, A Indar, C Bunce, and A Tyers. Repeatability and reproducibility of upper eyelid measurements. *The British Journal of Ophthalmology*, 85(1):99–101, 2001.
- [6] Riddhish Bhalodia, Lucas A. Dvoracek, Ali M. Ayyash, Ladislav Kavan, Ross Whitaker, and Jesse A. Goldstein. Quantifying the severity of metopic craniosynostosis: A pilot study application of machine learning in craniofacial surgery. *Journal of Craniofacial Surgery*, 31(3):697, 2020.
- [7] Lixia Lou, Longzhao Yang, Xin Ye, Yan Zhu, Shaoze Wang, Lingling Sun, Dahong Qian, and Juan Ye. A novel approach for automated eyelid measurements in blepharoptosis using digital image analysis. *Current Eye Research*, 44(10):1075–1079, 2019.
- [8] Alexandra Van Brummen, Julia P. Owen, Theodore Spaide, Colin Froines, Randy Lu, Megan Lacy, Marian Blazes, Emily Li, Cecilia S. Lee, Aaron Y. Lee, and Matthew Zhang. PeriorbitAI: Artificial intelligence automation of eyelid and periorbital measurements. *American Journal of Ophthalmology*, 230:285–296, 2021.
- [9] Jing Cao, Lixia Lou, Kun You, Zhiyuan Gao, Kai Jin, Ji Shao, and Juan Ye. A novel automatic morphologic analysis of eyelids based on deep learning methods. *Current Eye Research*, 46(10):1495–1502, 2021. Publisher: Taylor & Francis _eprint: <https://doi.org/10.1080/02713683.2021.1908569>.
- [10] Roxana Fu, Andriy Bandos, Joseph K. Leader, Samyuktha Melachuri, Tejus Pradeep, Aashim Bhatia, Srikala Narayanan, Ashley A. Campbell, Matthew Zhang, José-Alain Sahel, and Jiantao Pu. Artificial intelligence automation of proptosis measurement: An indicator for pediatric orbital abscess surgery. *Ophthalmology and Therapy*, 12(5):2479–2491, 2023.
- [11] Khizar Rana, Mark Beecher, Carmelo Caltabiano, Carmelo Macri, Yang Zhao, Johan Verjans, and Dinesh Selva. Artificial intelligence to automate assessment of ocular and periocular measurements. *European Journal of Ophthalmology*, page 11206721241249773, 2024. Publisher: SAGE Publications.
- [12] Hung-Chang Chen, Shin-Shi Tzeng, Yen-Chang Hsiao, Ruei-Feng Chen, Erh-Chien Hung, and Oscar K. Lee. Smartphone-based artificial intelligence-assisted prediction for eyelid measurements: Algorithm development and observational validation study. *JMIR mHealth and uHealth*, 9(10):e32444, 2021. Company: JMIR mHealth and

uHealth Distributor: JMIR mHealth and uHealth Institution: JMIR mHealth and uHealth Label: JMIR mHealth and uHealth Publisher: JMIR Publications Inc., Toronto, Canada.

- [13] Alexander Kirillov, Eric Mintun, Nikhila Ravi, Hanzi Mao, Chloe Rolland, Laura Gustafson, Tete Xiao, Spencer Whitehead, Alexander C. Berg, Wan-Yen Lo, Piotr Dollár, and Ross Girshick. Segment anything, 2023.
- [14] Cheng-Han Lee, Ziwei Liu, Lingyun Wu, and Ping Luo. MaskGAN: Towards diverse and interactive facial image manipulation, 2020.
- [15] Debbie S. Ma, Joshua Correll, and Bernd Wittenbrink. The chicago face database: A free stimulus set of faces and norming data. *Behavior Research Methods*, 47(4), 2015.
- [16] Debbie S. Ma, Justin Kantner, and Bernd Wittenbrink. Chicago face database: Multiracial expansion. *Behavior Research Methods*, 53(3):1289–1300, 2021.
- [17] Anjana Lakshmi, Bernd Wittenbrink, Joshua Correll, and Debbie S. Ma. The india face set: International and cultural boundaries impact face impressions and perceptions of category membership. *Frontiers in Psychology*, 12, 2021. Publisher: Frontiers.
- [18] Yury Kartynnik, Artsiom Ablavatski, Ivan Grishchenko, and Matthias Grundmann. Real-time facial surface geometry from monocular video on mobile GPUs. *arxiv*, 2019.
- [19] Parisa Farmanifard and Arun Ross. Iris-SAM: Iris segmentation using a foundation model, 2024.
- [20] Ji Shao, Xingru Huang, Tao Gao, Jing Cao, Yaqi Wang, Qianni Zhang, Lixia Lou, and Juan Ye. Deep learning-based image analysis of eyelid morphology in thyroid-associated ophthalmopathy. *Quantitative Imaging in Medicine and Surgery*, 13(3):1592604–1591604, 2023. Publisher: AME Publishing Company.
- [21] Nickisa M. Hodgson and Fatemeh Rajaii. Current understanding of the progression and management of thyroid associated orbitopathy: A systematic review. *Ophthalmology and Therapy*, 9(1):21–33, 2020.
- [22] Xiao Huang, Lie Ju, Jian Li, Linfeng He, Fei Tong, Siyu Liu, Pan Li, Yun Zhang, Xin Wang, Zhiwen Yang, Jianhao Xiong, Lin Wang, Xin Zhao, Wanji He, Yelin Huang, Zongyuan Ge, Xuan Yao, Weihua Yang, and Ruili Wei. An intelligent diagnostic system for thyroid-associated ophthalmopathy based on facial images. *Frontiers in Medicine*, 9:920716, 2022.
- [23] Justin Karlin, Lisa Gai, Nathan LaPierre, Kayla Danesh, Justin Farajzadeh, Bea Palileo, Kodi Taraszka, Jie Zheng, Wei Wang, Eleazar Eskin, and Daniel Rootman. Ensemble neural network model for detecting thyroid eye disease using external photographs. *The British Journal of Ophthalmology*, 107(11):1722–1729, 2023.
- [24] Zhongwen Li, Wei Qiang, Hongyun Chen, Mengjie Pei, Xiaomei Yu, Layi Wang, Zhen Li, Weiwei Xie, Xuefang Wu, Jiewei Jiang, and Guohai Wu. Artificial intelligence to detect malignant eyelid tumors from photographic images. *npj Digital Medicine*, 5(1):1–9, 2022. Publisher: Nature Publishing Group.
- [25] Tae Keun Yoo, Joon Yul Choi, and Hong Kyu Kim. A generative adversarial network approach to predicting postoperative appearance after orbital decompression surgery for thyroid eye disease. *Computers in Biology and Medicine*, 118:103628, 2020.
- [26] null YixinQu, null BingyingLin, null ShuilingLi, null XianchaiLin, null ZhenMao, null XingyiLi, null RongxinChen, and null DanpingHuang. Effect of multichannel convolutional neural network-based model on the repair and aesthetic effect of eye plastic surgery patients. *Computational and Mathematical Methods in Medicine*, 2022:5315146, 2022.
- [27] Jiashuo Liu, Zheyen Shen, Yue He, Xingxuan Zhang, Renzhe Xu, Han Yu, and Peng Cui. Towards out-of-distribution generalization: A survey, 2023.
- [28] Nooshin Mojab, Philip S. Yu, Joelle A. Hallak, and Darvin Yi. CvS: Classification via segmentation for small datasets, 2021.

6 Supplemental Figures

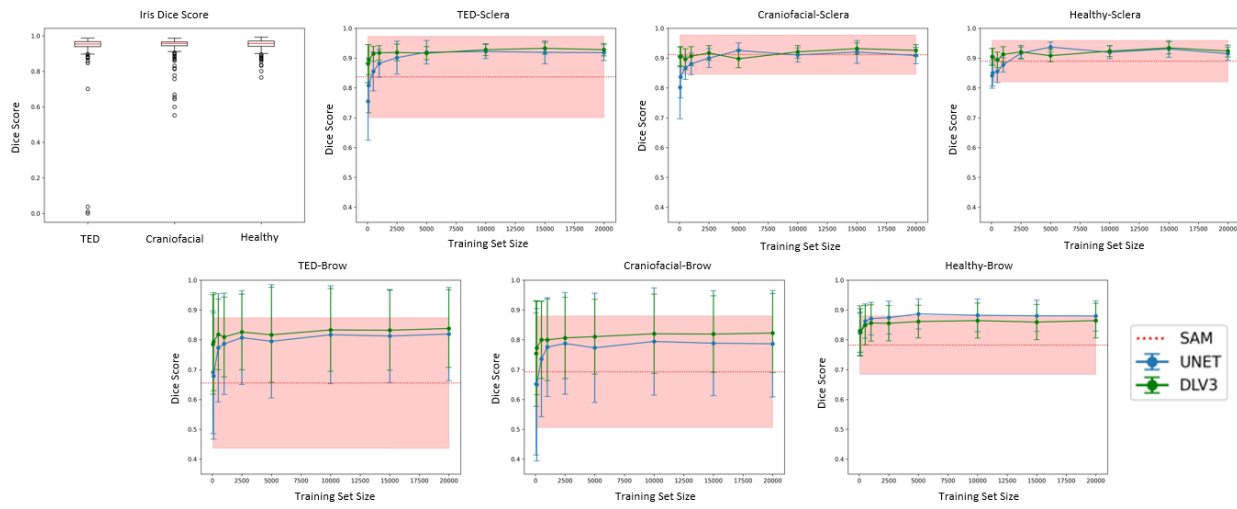


Figure 5: A) Dice score for SAM iris segmentation on all three datasets. Red line indicates the median, and the lines indicate the upper and lower quartiles. B-D) Dice scores for sclera and E-G) brow segmentation on all three datasets using SAM, as well as a UNET and DeepLabV3 when trained on increasingly large datasets. The red line indicates average SAM dice score, red shade indicates the standard deviation across the entire dataset. Blue (UNET) and green (DeepLabV3) lines and bars respectively denote the average and standard deviation segmentation at all of the training sizes evaluated.

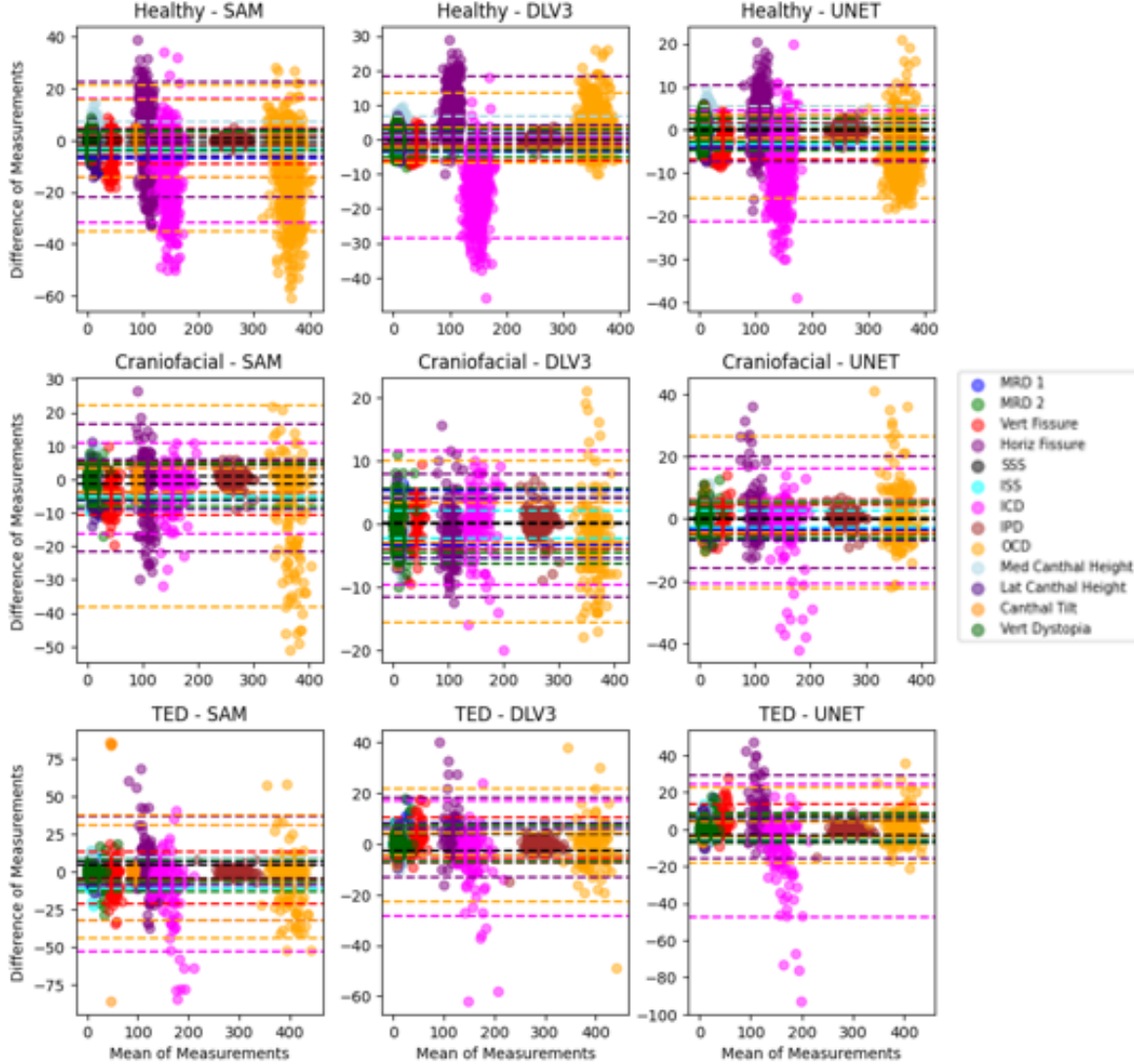


Figure 6: Bland Altman plots for the predicted eye distances from the human annotated images and from all of our models for all of our datasets. These plots were generated using the pixel level distances. Bilateral distances were averaged, and dashed lines represent the 95% limits of agreement (mean difference ± 1.96 standard deviations). Abbreviations can be interpreted as follows: MRD-Margin to Reflex Distance, ICD-inner canthal distance, IPD-interpupillary distance, OCD- outer canthal distance, ISS- inferior scleral show, SSS- superior scleral show, Vert Fissure- vertical palpebral fissure, Horiz Fissure- horizontal palpebral fissure, Med Canthal- medial canthal height, Lat Canthal- lateral canthal height.

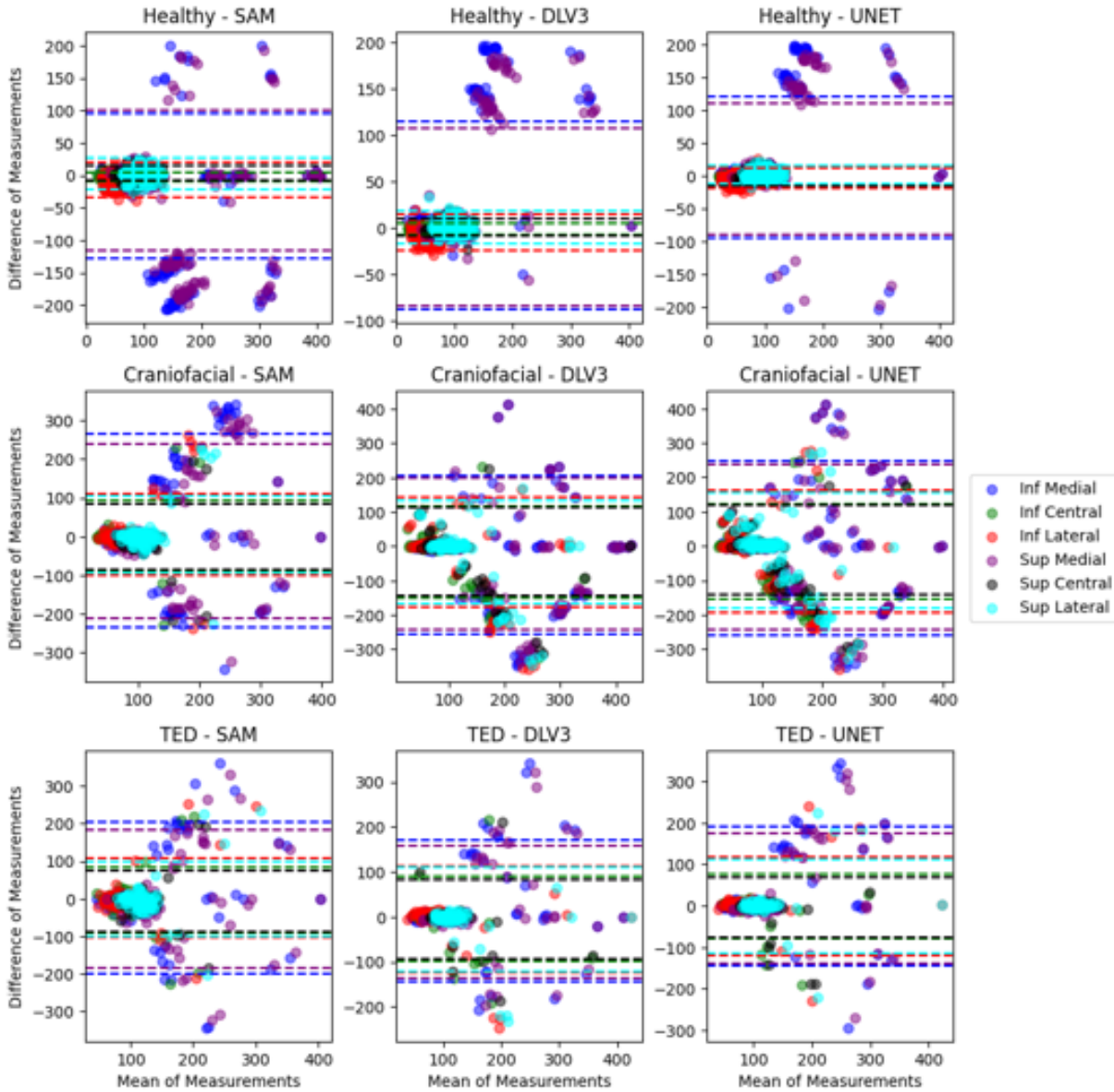


Figure 7: Bland Altman plots for the predicted brow distances from the human annotated images and from all of our models for all of our datasets. These plots were generated using the pixel level distances. Bilateral distances were averaged, and dashed lines represent the 95% limits of agreement (mean difference ± 1.96 standard deviations). Abbreviations can be interpreted as follows: Sup. Medial- superior medial brow height, Sup. Central- superior central brow height, Sup. Lateral- superior lateral brow height, Inf. Medial- inferior medial brow height, Inf. Central- inferior central brow height, Inf. Lateral- inferior lateral brow height.

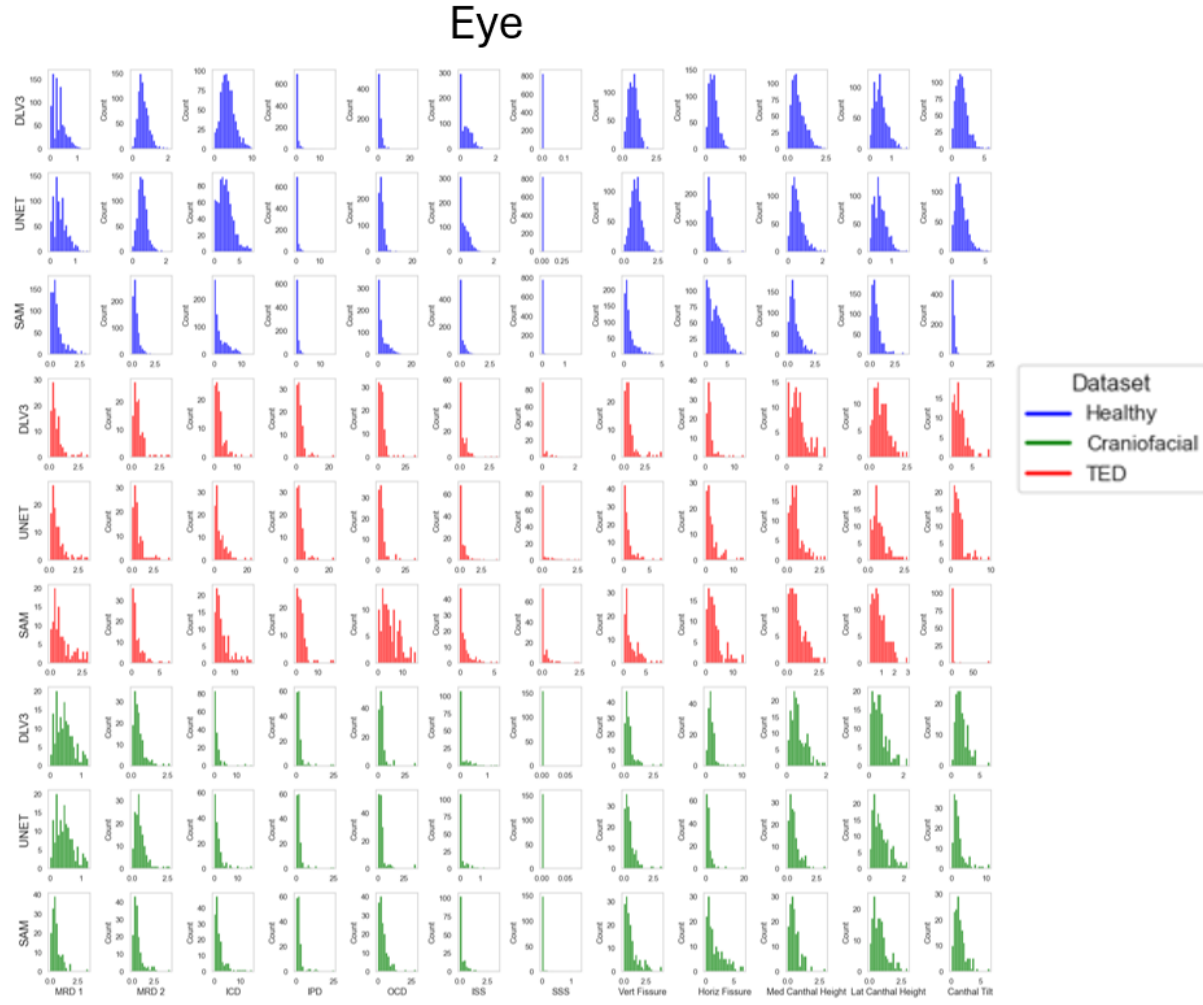


Figure 8: Histograms of MAE for all eye measurements using all models for all datasets. Bilateral distances were averaged. Scale is in mm following conversion using the iris as a diameter.

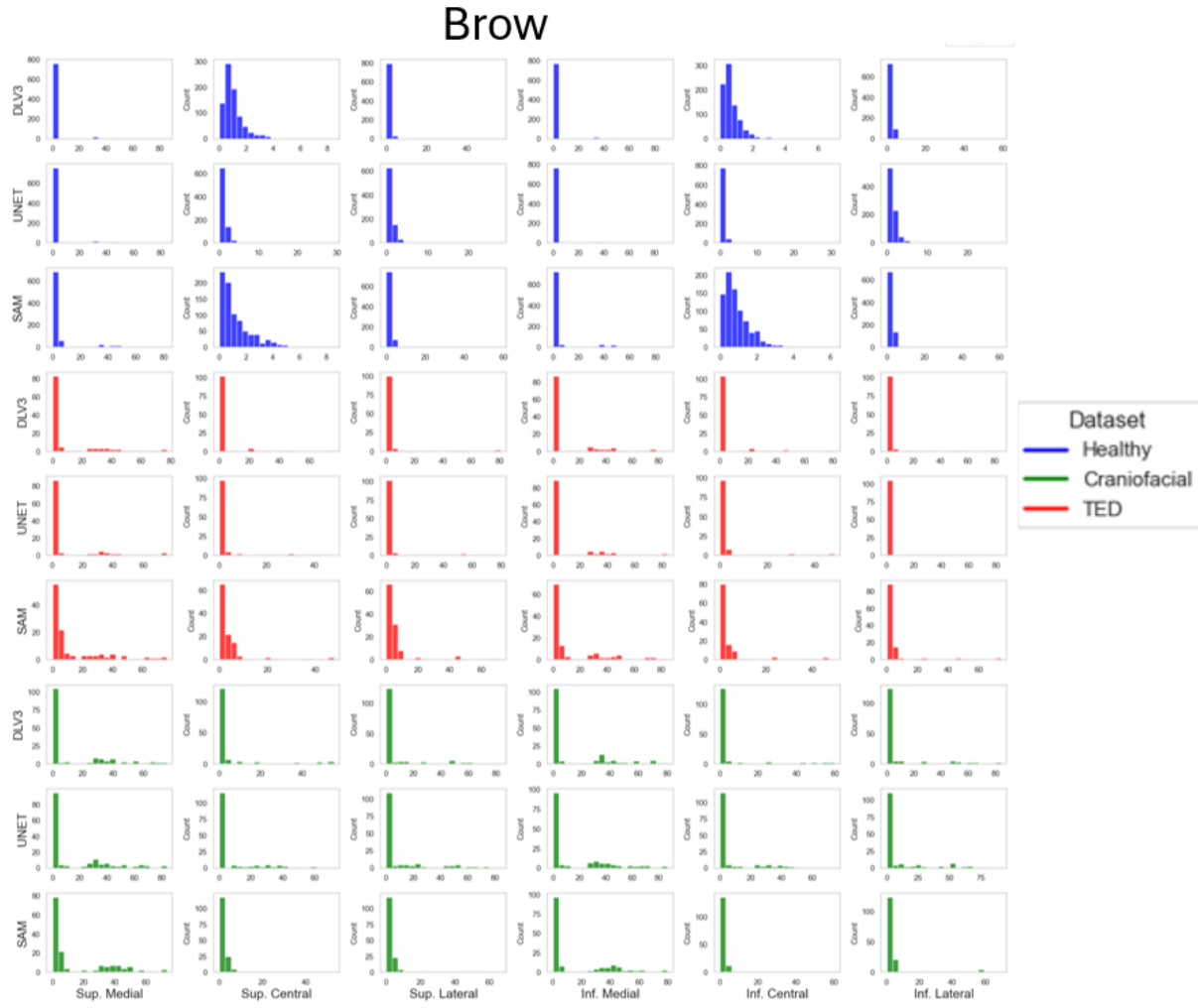


Figure 9: Histograms of MAE for all brow measurements using all models for all datasets. Bilateral distances were averaged. Scale is in mm following conversion using the iris as a diameter.

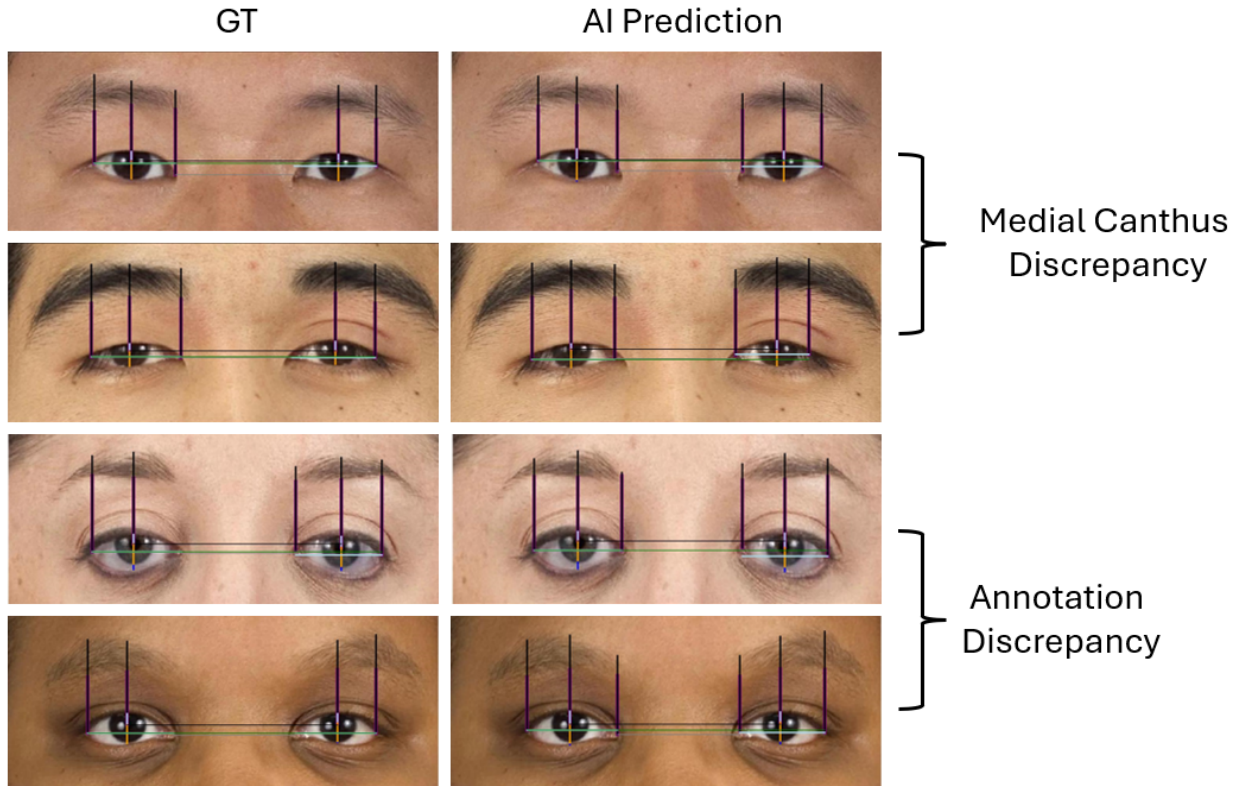


Figure 10: Representative examples of brow height discrepancies resulting from either human annotator judgment of medial brow margin or insufficient medial scleral segmentation.

7 Supplemental Tables

Dataset	Model	MRD 1	MRD 2	ICD	IPD	OCD	ISS	SSS	Vert. PF	Horiz PF	Canthal Tilt	Lat Canthal Height	Med Canthal Height	Vert Dystopia
Craniofacial	DLV3	4.52	5.16	3.25	5.81	6.45	5.19	0.00	4.52	5.19	4.52	4.52	5.16	5.16
	SAM	2.60	7.10	3.90	8.39	4.52	4.55	0.65	7.74	5.81	7.74	5.81	7.10	7.10
	UNET	4.52	5.16	6.45	5.81	3.90	5.19	0.00	5.16	4.55	5.81	7.74	7.10	5.16
Healthy	DLV3	5.93	4.96	4.84	6.08	4.36	4.00	0.00	3.75	5.32	5.32	4.59	5.44	9.07
	SAM	6.42	4.85	6.90	1.46	7.26	4.52	1.96	5.58	4.36	0.00	4.84	6.17	8.84
	UNET	6.53	6.17	4.36	6.08	4.36	4.96	0.00	4.84	4.72	4.35	4.72		9.07
TED	DLV3	6.19	4.42	5.31	1.79	3.57	2.70	2.68	6.19	5.31	6.19	6.19	6.19	0.89
	SAM	7.96	4.42	7.96	2.68	5.31	7.96	6.25	5.31	7.96	4.42	4.42	6.19	2.65
	UNET	7.08	5.31	3.54	1.79	4.46	5.36	5.31	6.19	7.08	7.96	5.31	7.08	0.89

Table 5: Percentage of Eye measurements outside the 95% limits of agreement (mean difference \pm 1.96 standard deviations) of bland altman plots for all models on all datasets. Bilateral distances were averaged. Abbreviations can be interpreted as follows: MRD-Margin Reflex Distance, ICD-inner canthal distance, IPD- interpupillary distance, OCD-outer canthal distance, ISS- inferior scleral show, SSS- superior scleral show, Vert Fissure- vertical palpebral fissure, Horiz Fissure- horizontal palpebral fissure, Med Canthal- medial canthal height, Lat Canthal- lateral canthal height.

Dataset	Model	Inf. Central	Inf. Lateral	Inf. Medial	Sup. Central	Sup. Lateral	Sup. Medial
Craniofacial	DLV3	7.10	8.39	9.03	6.45	8.39	9.68
	SAM	3.25	5.81	9.03	3.25	3.90	9.68
	UNET	7.74	9.68	7.74	7.74	9.68	7.74
Healthy	DLV3	3.27	0.24	5.02	4.60	0.36	4.90
	SAM	4.13	0.36	8.67	6.67	0.12	8.67
	UNET	0.12	1.45	5.52	0.73	0.97	5.40
TED	DLV3	5.36	2.70	10.62	4.46	2.70	10.62
	SAM	6.19	4.46	7.08	4.46	3.57	7.08
	UNET	3.60	3.60	7.08	4.46	3.60	7.96

Table 6: Percentage of brow measurements outside the 95% limits of agreement (mean difference \pm 1.96 standard deviations) of bland altman plots for all models on all datasets. Bilateral distances were averaged. Abbreviations can be interpreted as follows: Sup. Medial- superior medial brow height, Sup. Central- superior central brow height, Sup. Lateral- superior lateral brow height, Inf. Medial- inferior medial brow height, Inf. Central- inferior central brow height, Inf. Lateral- inferior lateral brow height.

		Sup. Medial	Sup. Central	Sup. Lateral	Inf. Medial	Inf. Central	Inf. Lateral
Healthy	UNET	4.39 ± 12.23	1.13 ± 1.56	1.12 ± 1.51	4.19 ± 13.17	0.71 ± 1.55	1.37 ± 1.62
	DLV3	4.23 ± 11.95	1.03 ± 0.80	1.12 ± 2.11	3.95 ± 12.74	0.67 ± 0.56	1.55 ± 2.30
	SAM	5.65 ± 12.91	1.22 ± 1.15	1.48 ± 3.00	5.74 ± 13.80	0.92 ± 0.74	2.09 ± 3.26
TED	UNET	9.56 ± 17.17	3.29 ± 8.49	4.88 ± 14.36	9.43 ± 18.67	3.26 ± 8.79	5.04 ± 14.84
	DLV3	10.41 ± 18.47	3.94 ± 10.39	4.71 ± 13.23	10.44 ± 19.64	3.65 ± 10.84	4.71 ± 13.55
	SAM	12.74 ± 18.50	4.45 ± 8.35	5.96 ± 11.40	13.18 ± 20.39	3.98 ± 8.89	5.41 ± 12.25
Craniofacial	UNET	16.11 ± 22.37	8.20 ± 14.58	11.22 ± 19.49	16.59 ± 23.34	8.13 ± 15.09	11.43 ± 20.13
	DLV3	13.74 ± 20.52	6.48 ± 13.23	7.80 ± 16.63	14.11 ± 21.64	6.23 ± 13.86	7.96 ± 17.44
	SAM	14.97 ± 19.73	3.26 ± 7.84	4.70 ± 11.08	15.91 ± 21.64	2.89 ± 8.54	4.88 ± 11.67

Table 7: Mean Absolute Error (MAE) of all models on all datasets used in this study for brow measurements. Outliers denote measurements that were greater than 1 standard deviation above the average MAE. MAE was calculated according to Equation 2, and is reported as +/- the standard deviation. Bold indicates the lowest MAE for each measurement for each model. Bilateral distances were averaged. Abbreviations can be interpreted as follows: Sup. Medial- superior medial brow height, Sup. Central- superior central brow height, Sup. Lateral- superior lateral brow height, Inf. Medial- inferior medial brow height, Inf. Central- inferior central brow height, Inf. Lateral- inferior lateral brow height.

		Sup. Medial	Sup. Central	Sup. Lateral	Inf. Medial	Inf. Central	Inf. Lateral
Healthy	UNET	1.28 ± 0.93	0.93 ± 0.55	0.92 ± 0.58	0.85 ± 0.58	0.61 ± 0.42	1.12 ± 0.72
	DLV3	1.33 ± 0.96	0.85 ± 0.39	0.97 ± 0.62	0.85 ± 0.62	0.53 ± 0.29	1.34 ± 0.93
	SAM	1.68 ± 1.49	0.83 ± 0.58	1.23 ± 0.96	1.47 ± 1.13	0.74 ± 0.39	1.80 ± 1.22
TED	UNET	2.66 ± 4.39	1.22 ± 1.33	1.42 ± 1.17	2.26 ± 5.55	1.11 ± 1.09	1.47 ± 0.95
	DLV3	3.28 ± 6.00	1.29 ± 1.02	1.79 ± 2.40	2.88 ± 6.40	0.91 ± 0.70	1.54 ± 1.62
	SAM	5.81 ± 7.74	2.54 ± 2.32	3.23 ± 2.63	5.54 ± 8.60	1.86 ± 1.83	2.40 ± 1.83
Craniofacial	UNET	7.25 ± 11.63	2.44 ± 4.36	3.96 ± 6.49	7.40 ± 12.27	1.78 ± 3.20	3.94 ± 6.59
	DLV3	5.42 ± 9.69	2.02 ± 3.26	2.20 ± 3.73	5.66 ± 10.78	1.38 ± 2.35	1.87 ± 2.77
	SAM	5.87 ± 9.42	1.79 ± 1.68	2.02 ± 1.73	5.68 ± 9.97	1.27 ± 1.13	2.03 ± 1.43

Table 8: Supplemental Table 4: Mean Absolute Error (MAE) of all models on all datasets used in this study for brow measurements with outliers excluded. Outliers denote measurements that were greater than 1 standard deviation above the average MAE (Equation 2). All measurements are reported as +/- the standard deviation. Bilateral distances were averaged. Bold indicates the lowest MAE for each measurement for each model. Abbreviations can be interpreted as follows: Sup. Medial- superior medial brow height, Sup. Central- superior central brow height, Sup. Lateral- superior lateral brow height, Inf. Medial- inferior medial brow height, Inf. Central- inferior central brow height, Inf. Lateral- inferior lateral brow height.

		Right		Left	
		Sup. Lateral	Sup. Medial	Sup. Lateral	Sup. Medial
Healthy	% Dataset periorbitAI	0.85		0.86	
	SAM	2.87 ± 2.32	6.68 ± 14.02	2.87 ± 2.49	7.04 ± 17.92
	UNET	1.34 ± 2.09	5.15 ± 14.79	1.65 ± 5.78	5.91 ± 18.85
	DLV3	1.14 ± 1.08	4.19 ± 13.18	0.98 ± 0.93	4.39 ± 16.22
TED	% Dataset periorbitAI	0.58		0.63	
	SAM	4.19 ± 8.18	6.46 ± 15.18	5.16 ± 12.02	9.63 ± 20.53
	UNET	4.27 ± 6.05	10.24 ± 18.31	3.55 ± 10.00	8.74 ± 20.53
	DLV3	1.96 ± 5.22	4.77 ± 11.74	4.40 ± 17.62	7.57 ± 19.47
Craniofacial	% Dataset periorbitAI	0.66		0.62	
	SAM	3.91 ± 7.68	10.57 ± 20.16	5.40 ± 16.24	6.95 ± 19.24
	UNET	2.62 ± 6.16	9.19 ± 18.93	4.05 ± 17.21	13.68 ± 28.65
	DLV3	2.92 ± 8.55	8.93 ± 19.54	6.95 ± 23.46	10.24 ± 25.14

Table 9: Comparison of MAE (computed using Equation 2) of our models to PeriorbitAI for brow measurements. For all measurements, for both our models and PeriorbitAI, MAE was computed using only images successfully analyzed by PeriorbitAI. ‘% Dataset’ denotes the percentage of the original dataset for each measurement successfully processed by PeriorbitAI. Bold denotes lowest MAE of each measurement for each dataset. Abbreviations can be interpreted as follows: Sup. Medial- superior medial brow height, Sup. Central- superior central brow height, Sup. Lateral- superior lateral brow height, Inf. Medial- inferior medial brow height, Inf. Central- inferior central brow height, Inf. Lateral- inferior lateral brow height.